Title

High sound pressure piezoelectric micromachined ultrasonic transducers using sputtered potassium sodium niobate.

Permalink

https://escholarship.org/uc/item/9qz9s8c2

Journal

Microsystems & Nanoengineering, 10(1)

Authors

Xia, Fan
Peng, Yande
Yue, Wei
et al.

Publication Date

2024-12-27

DOI

10.1038/s41378-024-00841-y

Peer reviewed

High sound pressure piezoelectric micromachined ultrasonic transducers using sputtered potassium sodium niobate

Fan Xia[1], Yande Peng [1], Wei Yue [1], Mingze Luo[2], Megan Teng[1], Chun-Ming Chen[1], Sedat Pala[1], Xiaoyang Yu[3], Yuanzheng Ma[4], Megha Acharya[5], Ryuichi Arakawa[6], Lane W. Martin [5,7] and Liwei Lin [1✉]

Abstract

This work presents air-coupled piezoelectric micromachined ultrasonic transducers (pMUTs) with high sound pressure level (SPL) under low-driving voltages by utilizing sputtered potassium sodium niobate $K_{0.34}Na_{0.66}NbO_3$ (KNN) films. A prototype single KNN pMUT has been tested to show a resonant frequency at 106.3 kHz under 4 V_{p-p} with outstanding characteristics: (1) a large vibration amplitude of 3.74 μm/V, and (2) a high acoustic root mean square (RMS) sound pressure level of 105.5 dB/V at 10 cm, which is 5–10 times higher than those of AlN-based pMUTs at a similar frequency. There are various potential sensing and actuating applications, such as fingerprint sensing, touch point, and gesture recognition. In this work, we present demonstrations in three fields: haptics, loudspeakers, and rangefinders. For haptics, an array of 15 × 15 KNN pMUTs is used as a non-contact actuator to provide a focal pressure of around 160.3 dB RMS SPL at a distance of 15 mm. This represents the highest output pressure achieved by an airborne pMUT for haptic sensation on human palms. When used as a loudspeaker, a single pMUT element with a resonant frequency close to the audible range at 22.8 kHz is characterized. It is shown to be able to generate a uniform acoustic output with an amplitude modulation scheme. In the rangefinder application, pulse-echo measurements using a single pMUT element demonstrate good transceiving results, capable of detecting objects up to 2.82 m away. As such, this new class of high-SPL and low-driving-voltage pMUTs could be further extended to other applications requiring high acoustic pressure and a small form factor.

Introduction

Ultrasonic transducers have been widely used in object detection[1], non-destructive testing (NDT)[2,3], biomedical imaging[4,5], and therapeutic treatments[6,7]. Compared with bulk ultrasonic transducers, piezoelectric micromachined ultrasonic transducers (pMUTs) with small footprints offer advantages of low power consumption and wide bandwidth for applications in consumer electronics and the Internet of Things (IoT), such as range-finding[8,9], gesture recognition[10,11], fingerprint sensing[12,13], and 3D

imaging[14,15]. However, these small sensors have relatively low output pressure, which limits signal transmission in various applications. For instance, the state-of-the-art AlN-based pMUT array has only achieved a travel distance of 4 m[16]. To extend pMUTs' use in applications, such as mid-air haptics[17–19], loudspeakers[20,21], and acoustic tweezers[22], the main challenge lies in achieving a high output sound pressure level (SPL).

The transmitting characteristics of pMUTs are primarily defined by the mechanical structural design and the active piezoelectric material, and the quest for better performance leads to a need for new materials. Extensive efforts have been made in optimizing the device structures, such as new design configurations[23,24], optimal diaphragm geometries[25–29], and modified boundary conditions[30–32]. For instance, F. Sammoura et al.[23]

Correspondence: Liwei Lin (lwlin@berkeley.edu)
[1]Department of Mechanical Engineering, University of California, Berkeley, CA 94720, USA
[2]School of Electronic Science and Engineering, Southeast University, Nanjing, Jiangsu 210096, China
Full list of author information is available at the end of the article
These authors contributed equally: Fan Xia, Yande Peng.

demonstrated a two-port pMUT with the differential driving scheme to double the acoustic power output per input voltage. S. Akhbari et al.[24] constructed the dual-electrode bimorph (DEB) architecture to realize a vibration displacement four times that of traditional single-electrode unimorph pMUTs. The mode shape of the diaphragm also affects the performance: flexurally-suspended membrane[25] and holes[26,27] could transform the mode shape from fully clamped to piston-like, which improves the transmission. Besides, experimental and theoretical work also shows that applying pinned-[31] or free-[32] boundary conditions can be beneficial. Aside from the structural design, the active piezoelectric material also plays an important role in the performance, which could be characterized by the piezoelectric coefficient e_{31f}. The most studied piezoelectric material, AlN, has a low e_{31f} of -1 C/m^2. The piezoelectric coefficient can be increased by tuning the material compositions[33-35]. For example, 36% scandium-substituted AlN (ScAlN) films[33] have an improved e_{31f} of around -2.3 C/m^2. Other materials, like lead zirconate titanate (PbZr$_{1-x}$Ti$_x$O$_3$ or PZT)[36,37], can produce relatively high output pressure, but the presence of lead and their low receiving sensitivity due to high dielectric constant raise concerns for use in real applications. As such, there is a need for new piezoelectric materials to further improve the pMUT performance.

Lead-free piezoelectric materials such as barium titanate (BaTiO$_3$)[38], lithium niobate (LiNbO$_3$)[39,40] and potassium sodium niobate (K,Na)NbO$_3$[41-43] have sparked extensive interest. For example, sol-gel-based KNN pMUT[44] has exhibited a 1.25 μm/V vibration amplitude under the resonance at 66.2 kHz. Meanwhile, sputtered KNN films[43] can be batch fabricated as the active layers in pMUTs[45]. Here, we report air-coupled pMUTs based on sputtered, lead-free K$_{0.34}$Na$_{0.66}$NbO$_3$ film with a high piezoelectric coefficient ($e_{31f} \approx -8$ to -10 C/m^2) and a relatively low dielectric constant ($\varepsilon_r \approx 260-300$). Results show an excellent transmission sensitivity as high as 105.5 dB/V at 10 cm away, which is 5-10 times higher than those of AlN-based pMUTs at a similar frequency. Potential applications in haptics, loudspeakers, and rangefinders have been demonstrated to highlight the advantages of such high-SPL KNN pMUTs. Specifically, (1) an array of 15 × 15 KNN pMUT elements is used to generate haptic stimulation at a frequency within human perception range through pulse-width modulation; (2) a single pMUT with a resonant frequency close to the audible range is tested as a loudspeaker by using the amplitude modulation (AM) scheme; and (3) good transceiving ability is demonstrated by using a single pMUT as an airborne rangefinder based on pulse-echo measurements.

Results and discussion
Design

There are three energy domains in a pMUT's transduction process: electrical, mechanical, and acoustic. PMUTs utilize electric-mechanical-acoustic coupling to convert electrical excitation signals into acoustic waves. As shown in Fig. 1a, the working diaphragm typically comprises a piezoelectric layer and an elastic layer, which is known as a unimorph diaphragm. When an external electric field is applied across the diaphragm, the piezoelectric layer generates in-plane strain through the converse piezoelectric effect. The elastic layer shifts the neutral plane of the entire layer stack away from the midplane of the piezoelectric layer, generating a bending moment that creates out-of-plane displacement[46,47]. When an alternating current (AC) voltage is applied, the diaphragm vibrates periodically in the transverse direction, which is known as the flexural mode. This mechanical vibration pushes the surrounding medium particles to vibrate and ultimately emits an acoustic wave into the environment. The electromechanical coupling coefficient, which indicates the proportion of the total input electrical energy stored as mechanical energy[47,48], is highly dependent on the piezoelectric coefficient e_{31f}. A higher e_{31f} results in a greater electromechanical coupling coefficient, inducing more energy to be converted into mechanical deformation. Therefore, the high e_{31f} value around -8 to -10 C/m^2 from the sputtered KNN film is beneficial for improving the transmission performance.

Here, the KNN pMUT is designed with a circular unimorph diaphragm consisting of a 2-μm-thick sensor-type KNN film[43,45] as the active piezoelectric layer and a 5-μm-thick silicon device layer as the elastic layer. The dual-electrode geometry features a circular-shaped inner electrode with a radius equal to 67% of the diaphragm radius and a ring-shaped outer electrode. A differential drive is applied by exciting the inner and outer electrodes with opposite polarity to enhance the vibration displacement and output pressure. The simulated fundamental flexural operation mode with the clamped boundary condition is shown in Fig. 1b. The inner and outer portions experience stress of opposite polarity (tensile or compressive) with the inflection point located at ~67% of the radius[47]. The differential drive configuration maximizes the use of the entire piezoelectric diaphragm for increased outputs.

Fabrication process

The detailed fabrication process is shown in Fig. 1c. The KNN film deposition process has been previously reported[43,45]. The pMUT fabrication starts with the deposition of a 25-nm-thick zinc oxide (ZnO) adhesion layer and a 200-nm-thick platinum (Pt) bottom electrode layer on a 6-inch silicon-on-insulator (SOI) wafer, which consists of
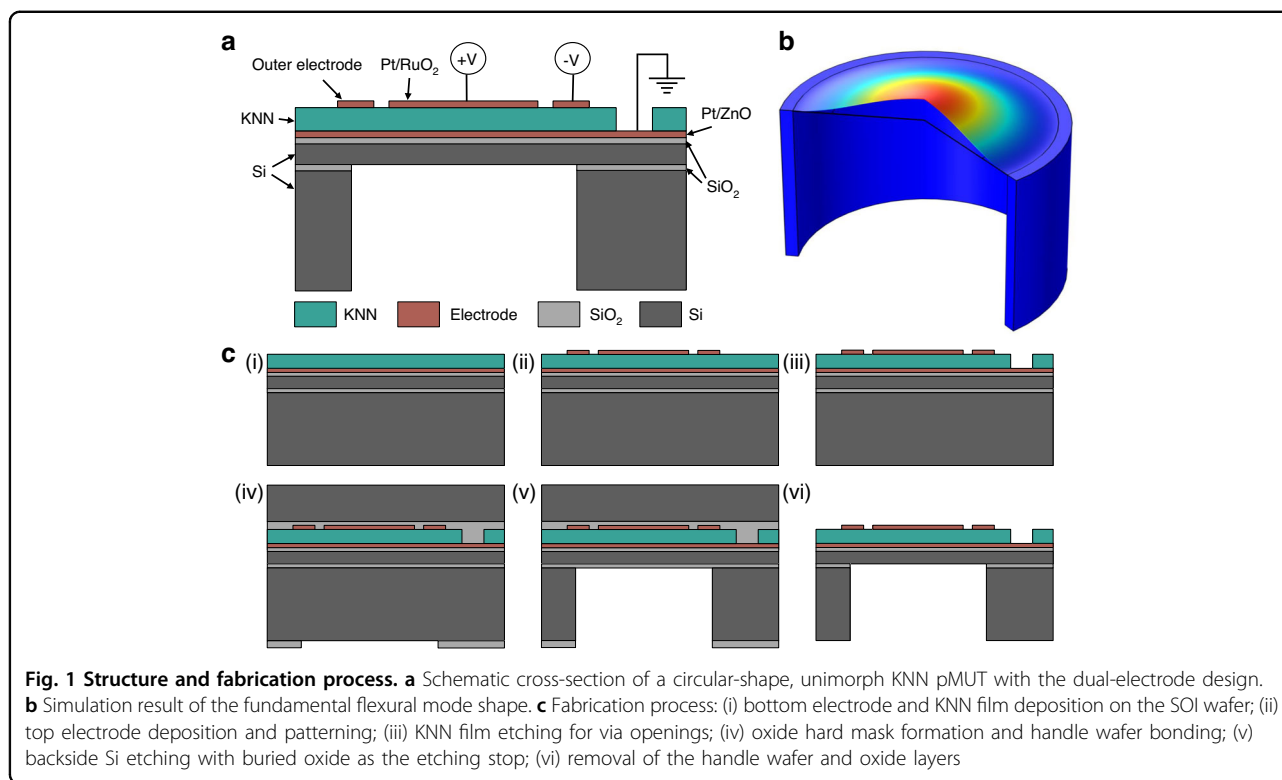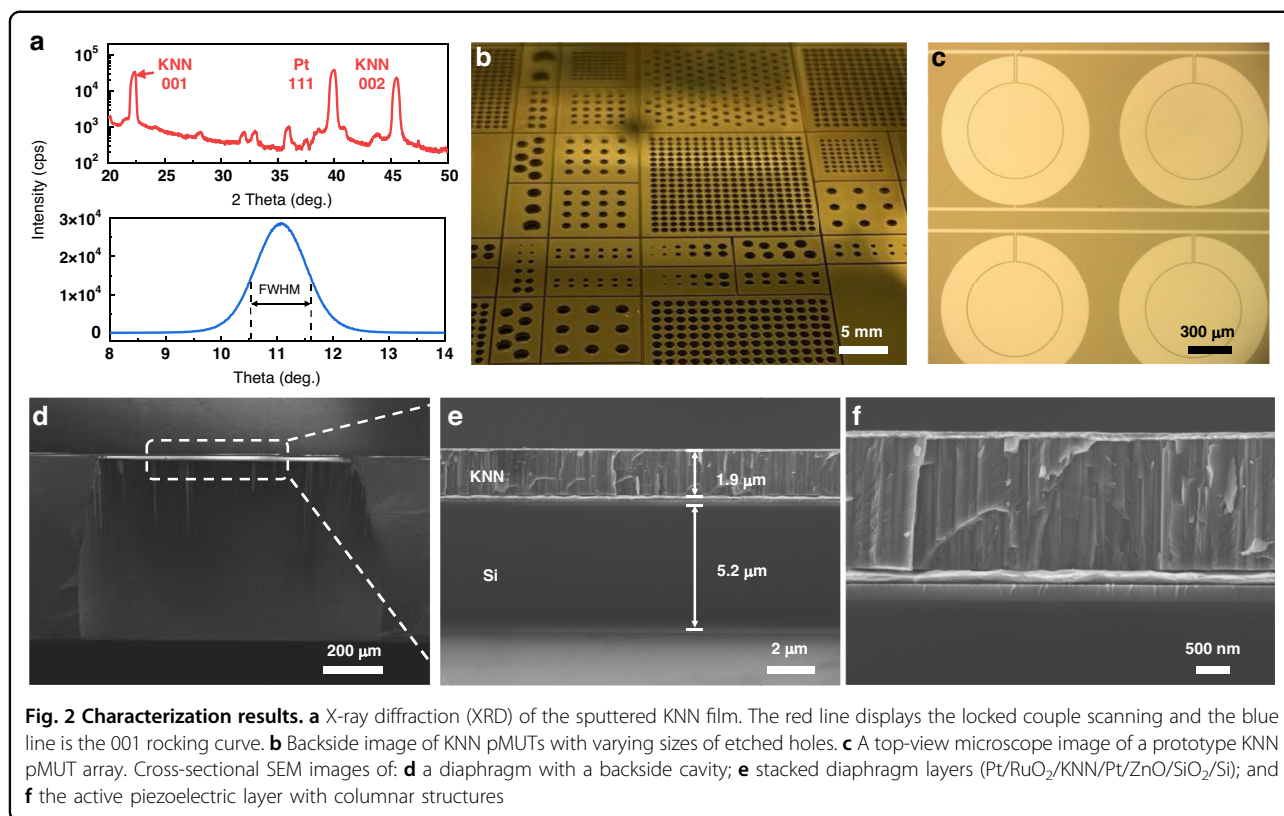
Fig. 1 Structure and fabrication process. a Schematic cross-section of a circular-shape, unimorph KNN pMUT with the dual-electrode design. **b** Simulation result of the fundamental flexural mode shape. **c** Fabrication process: (i) bottom electrode and KNN film deposition on the SOI wafer; (ii) top electrode deposition and patterning; (iii) KNN film etching for via openings; (iv) oxide hard mask formation and handle wafer bonding; (v) backside Si etching with buried oxide as the etching stop; (vi) removal of the handle wafer and oxide layers

a 5-μm-thick silicon (Si) device layer with a 200-nm-thick thermal oxide layer, 1-μm-thick buried silicon oxide (BOX) layer and a 610-μm-thick (100) Si handle substrate. A 2-μm-thick KNN film, serving as the active piezoelectric layer, is then deposited via a radio frequency (RF) magnetron-sputtering process at 500 °C on top of the Pt/ZnO bottom electrode layer. A stoichiometric $(K_{0.32} Na_{0.68})NbO_3$ ceramic material with less than 0.4 at.% of Cu and/or Mn is used as the sputtering target[43]. Subsequently, a 10-nm-thick ruthenium oxide (RuO_2) layer and a 100-nm-thick Pt layer are sputtered and patterned as the inner circular and outer ring top electrodes, where RuO_2 is used to promote the adhesion strength between the Pt and KNN film. The opening vias to access the bottom electrode are created by patterning the KNN film through a wet-etching process, using an etchant solution consisting of hydrogen peroxide (H_2O_2), ammonium hydroxide (NH_4OH), and hydroxyethylidene diphosphonic acid (HEDP) in a 75 °C water bath. Finally, the backside silicon cavity is defined by a silicon deep reactive-ion etching (DRIE) process. Before the DRIE process, a layer of silicon oxide is deposited onto the frontside of the device wafer as a protection layer, while another layer of silicon oxide is deposited and then patterned as a hard mask on the backside of the device wafer. The device wafer is then temporarily bonded to a 6-inch, 675-μm-thick Si handle wafer using the adhesive polymer (Santovac vacuum fluid), with the backside of the device wafer facing outward for backside etching. The DRIE process is conducted using the STS2 Inductively Coupled Plasma (ICP) etch system, with alternating cycles of etching and protective polymer deposition to achieve a high aspect ratio. Specifically, octafluorocyclobutane (C_4F_8) is used as the passivation gas, while sulfur hexafluoride (SF_6) and oxygen (O_2) are used as the etchant gases. The BOX layer works as the etching stop layer due to the high etching selectivity between silicon and silicon oxide. Finally, the device wafer is debonded from the handle wafer through a 2-min treatment on a 90 °C hotplate, and dies of various designs are separated. The residual Santovac vacuum fluid is cleaned sequentially with acetone, isopropyl alcohol (IPA), and deionized (DI) water. Any residual buried oxide, frontside oxide, and backside oxide are removed by the buffered hydrofluoric acid (HF) treatment to release the device.

Characterization

Figure 2 presents the characterization results of the fabricated KNN pMUTs. The crystal structure of the sputtered KNN film is examined by using X-ray diffraction (XRD), as shown in Fig. 2a. The locked couple scanning results show the 001 and 002 diffraction peaks of the KNN layer, as well as the 111 diffraction peak of the Pt electrode. The full-width at half-maximum (FWHM) measured from the rocking curve about the 001 diffraction condition is ~1.08°, which confirms the good

Fig. 2 Characterization results. a X-ray diffraction (XRD) of the sputtered KNN film. The red line displays the locked couple scanning and the blue line is the 001 rocking curve. **b** Backside image of KNN pMUTs with varying sizes of etched holes. **c** A top-view microscope image of a prototype KNN pMUT array. Cross-sectional SEM images of: **d** a diaphragm with a backside cavity; **e** stacked diaphragm layers (Pt/RuO$_2$/KNN/Pt/ZnO/SiO$_2$/Si); and **f** the active piezoelectric layer with columnar structures

crystallinity of the KNN film. Figure 2b shows the backside image of pMUT devices with various hole sizes, demonstrating the flexibility in design and fabrication for devices with different resonant frequencies. The optical top-view image of pMUTs (Fig. 2c) highlights the benign surface morphology. The cross-sectional scanning electron microscope (SEM) images in Fig. 2d–f display the well-defined backside silicon cavity, the tightly stacked Pt/RuO$_2$/KNN/Pt/ZnO/SiO$_2$/Si multi-layered diaphragm structure, and the thickness of each layer (1.9-μm-thick KNN and 5.2-μm-thick Si device layer). Figure 2f presents a zoomed-in image of the active layer, where the dense columnar structure of the KNN film validates good crystal orientation for the high-quality films. Additionally, due to imperfections in the backside etching process, deviations exist between the actual and designed diaphragm radius (500 μm), as illustrated in Fig. 2d. For simulation and theoretical analysis in the next section, a diaphragm radius of 420 μm is used as an example.

Electrical characterization

The electrical impedance characteristics of single KNN pMUT elements are measured by an impedance analyzer under 2 V$_{p-p}$. As the diaphragm radius increases from 300 to 1200 μm, the resonant frequency decreases from 241 to 21.2 kHz in Fig. 3a. This decrease is attributed to the inverse relationship between the resonant frequency of

the diaphragm under flexural mode and the square of the diaphragm radius[47]. The deviations between the simulation and experimental results are attributed to differences in the actual diaphragm radius, as well as the residual stress within the films. Notably, the simulated results for a radius of 400–420 μm closely match the measured resonant frequency with the designed radius of 500 μm. The impedance and phase versus frequency curves of a pMUT element (500 μm in radius) obtained under a 200 mV$_{p-p}$ excitation across its inner electrode and bottom electrode is shown in Fig. 3b. A resonant frequency f_r of 99.29 kHz and an anti-resonant frequency f_a of 100.79 kHz are observed. The electromechanical coupling factor k_t^2 is calculated to be 3.62% based on the following equation[35]:

$$k_t^2 = \frac{\pi^2}{4} \frac{f_r}{f_a} \frac{f_a - f_r}{f_a} \tag{1}$$

As such, the electromechanical coupling factor of the unimorph, clamped KNN pMUT is ~2.5 times higher than that of AlN-based pMUTs (~1%) and about 1.8 times that of ScAlN-based pMUTs (~2%)[34,35].

Mechanical characterization

The mechanical vibration behavior of the KNN pMUT (500 μm in radius) under the differential driving scheme is

Fig. 3 Electrical, mechanical, and acoustic characterizations. a Simulated (blue) and measured (red) resonant frequencies for different elements. **b** Measured impedance and phase versus frequency for a 500-μm-radius pMUT driven by a 200 mV$_{p-p}$ voltage at the inner electrode. **c** Simulated (blue) and measured (red) center displacement of a pMUT (500 μm in radius) under a 200 mV$_{p-p}$ differential driving. **d** Measured center displacement and velocity versus frequency under various excitation voltages (200 mV$_{p-p}$, 500 mV$_{p-p}$, 1 V$_{p-p}$, 4 V$_{p-p}$) with the differential driving scheme. **e** Resonant frequency, center displacement, displacement sensitivity, and quality factor versus driving voltage. **f** Measured (red) and fitted (blue, to Eq. (3)) resonant frequency with respect to peak displacement. **g** Measured root mean square (RMS) sound pressure level versus frequency under the differential driving scheme at a 1 cm axial distance. **h** Measured (red) and fitted (blue, to Eq. (4)) RMS sound pressure level versus axial propagation distance at 106.3 kHz under 4 V$_{p-p}$. **i** Transmission performance for state-of-the-art pMUTs

characterized using a single-beam laser Doppler vibrometer (LDV, Polytec VibroOne) with continuous sine-wave excitation. Detailed information is available in the "Experimental setup" section. Figure 3c displays both the simulated and measured frequency response of the displacement amplitude at the center of the diaphragm under a 200 mV$_{p-p}$ excitation. This center position also corresponds to the point of maximum displacement across the diaphragm in the fundamental mode shape. Model details are described in the "Simulation method" section. A symmetrical frequency response is observed in

both cases, and the measured displacement reaches 1.23 μm under a driving voltage of only 200 mV$_{p-p}$, corresponding to a displacement sensitivity of 12.3 μm per volt (μm/V). The deviations between the simulation and experimental results are attributed to differences in the actual diaphragm radius, residual stress within the films, mechanical and piezoelectric material properties. Figure 3d further illustrates the mechanical performance under various excitation voltages, including 200 mV$_{p-p}$, 500 mV$_{p-p}$, 1 V$_{p-p}$, and 4 V$_{p-p}$. Both displacement and velocity increase with voltage. The center displacement at

resonance under $4\,V_{p-p}$ can reach $7.48\,\mu m$, showing a high displacement sensitivity of $3.74\,\mu m/V$, which is 3.3 times higher than that of a 36% scandium-substituted AlN pMUT ($0.86\,\mu m/V$ at $85\,kHz$)[33]. This result also matches well with the theoretical predictions based on the piezo-electric coefficient $e_{31,f}$. The frequency response gradually becomes asymmetrical as the voltage increases, where the nonlinear hardening behavior can be observed starting from $500\,mV_{p-p}$, which is caused by the membrane tensioning effect[49].

The impacts of driving voltage on resonant frequency, center displacement at resonance, displacement sensitivity, and quality factor are summarized in Fig. 3e. With increased driving voltage, the resonance shifts from 98.7 to $106.3\,kHz$. The corresponding displacement increases from 1.23 to $7.48\,\mu m$, while displacement sensitivity is reduced from 12.3 to $3.74\,\mu m/V$, indicating the reduced driving efficiency in the nonlinear region. The quality factor (Q) also decreases from around 41 to around 11 correspondingly, indicating a larger damping and faster mechanical-acoustic energy transfer process.

We further investigate the nonlinear behavior of the pMUT, which is found to be dominated by Duffing nonlinearity ($k_3 x^3$). Therefore, the governing equation of motion can be described as[50]:

$$\ddot{x} + 2(\zeta_1 + \zeta_3 x^2)\omega_0\dot{x} + \omega_0^2 x + \frac{k_3}{m_{eff}} x^3 = \frac{F_{ext}}{m_{eff}} \qquad (2)$$

where $\omega_0 = 2\pi f_0$ is the angular eigenfrequency of the fundamental flexural mode; m_{eff} is the effective modal mass of the device; F_{ext} is the external driving force on the pMUT; $k_3[N/m^3]$ is the coefficient of the conservative Duffing nonlinearity; ζ_1 is the linear damping coefficient; and $\zeta_3[m^{-2}]$ is the third order nonlinear damping coefficient. The nonlinear stiffness term involving k_3 induces amplitude-dependent frequency drift, as observed in Fig. 3d. Meanwhile, the nonlinear damping term involving ζ_3 creates amplitude-dependent decay, which results in the Q variation. By solving the differential equation, we can deduce the steady-state resonant frequency under increasing displacement r:

$$\omega = \omega_0 + \frac{3k_3 r^2}{8\omega_0 m_{eff}} \qquad (3)$$

Figure 3f depicts the nonlinear behavior of the pMUT in the resonant frequency versus the peak displacement plot. Equation (3) is used to fit the measurement results. In the equation, the angular eigenfrequency $\omega_0 = 2\pi f_0$ is derived using the eigenfrequency ($f_0 = 98.7kHz$) extracted from Fig. 3d when the pMUT is operating within the linear region. The effective modal mass ($m_{eff} = 2.71 \times 10^{-9} kg$) is calculated as $m_{eff} = 0.184\pi a^2 \sum_{i=1} \rho_i h_i$, where a is the radius of the pMUT, and ρ_i, h_i denote the

density and thickness of the i_{th} layer respectively (cross-section shown in Fig. 1a). The coefficient 0.184 is derived from the lumped parameter when equating the flexural mode pMUT to a piston vibrator[47]. Subsequently, we fix the ω_0 and m_{eff} in the equation to fit the observed nonlinear behavior in Fig. 3f and the Duffing coefficient k_3 is extracted from the optimal fitting result as $3.9 \times 10^{12} N/m^3$. This coefficient primarily arises from geometrical nonlinearity, which can be expressed as $k_3 = \frac{6.24\pi h E_Y}{d^2} \frac{13+21\nu-4\nu^2}{30(1+\nu)}$, where h, d, E_Y, and ν are thickness, diameter, Young's modulus, and Poisson's ratio of the diaphragm materials[51], respectively.

Transmission performance

The transmission pressure of the prototype KNN pMUT ($500\,\mu m$ in radius) under the continuous differential sine-wave driving is evaluated using a high-sensitivity microphone (Bruel & Kjar, Type 4138). The receiving signal is collected by placing the microphone $1\,cm$ above the pMUT, and the root mean square (RMS) sound pressure level (SPL) is extracted, as shown in Fig. 3g. Detailed setup and calculations are provided in the "Experimental setup" section. The transmission pressure behaviors are similar to those of mechanical characteristics. As the transmission pressure increases with a high driving voltage, the resonant frequency also increases. A maximum transmission pressure of $133\,dB$ RMS SPL is achieved at $105.4\,kHz$ with a $4\,V_{p-p}$ drive voltage. The effect of axial propagation distance on transmission pressure is further evaluated at $4\,V_{p-p}$, as shown in Fig. 3h. The transmission pressure gradually decreases from $139.5\,dB$ at $0.4\,cm$ to $132.3\,dB$ at $1\,cm$, and $111.6\,dB$ at $10\,cm$ (at the resonance of $106.3\,kHz$ during testing). Thus, the transmission sensitivity of the single KNN pMUT reaches $126.3\,dB/V$ RMS SPL at $1\,cm$ and $105.5\,dB/V$ RMS SPL at $10\,cm$ axial distance. The output pressure decays exponentially as the distance R increases, and this matches well with the theoretical model[52]:

$$p(R) = \frac{\rho f_0 S_T V_T}{R} 10^{-\alpha R} \qquad (4)$$

where ρ is the medium density; S_T is the output volume velocity sensitivity of pMUT; V_T is the transmit voltage; and α is the attenuation coefficient under operating frequency f_0.

A summary of the transmission performance comparison with other devices in the state-of-the-art literature is presented in Fig. 3i and Table 1. The sound pressure level correlates with the operation frequency (resonant frequency). A high operation frequency can yield a high output pressure but also experiences large attenuation (large attenuation coefficient α) during propagation. These characteristics make it challenging to evaluate

Table 1 Transmission sensitivity comparison with other devices in the state-of-the-art literature

Material	Frequency	V_{p-p}	SPL (dB)	SPL (dB/V)	Distance (cm)	Year	Ref.
AlN	101k	20	110	90	10	2021	[14]
AlN	35.3k	32	89.9	65.8	1.05	2020	[76]
PZT	100k	6	103	93.5	3.5	2017	[37]
PZT	482k	2	63.7	63.7	1	2016	[77]
PMN-PZT	151k	3	98.1	94.6	6	2017	[78]
PVDF	121.5k	10	100.4	86.4	1	2018	[19]
KNN	**106.3k**	**4**	**132.3**	**126.3**	**1**	**This work**	
KNN	**106.3k**	**4**	**111.6**	**105.5**	**10**	**This work**	
KNN	**22.8k**	**4**	**105**	**99**	**3**	**This work**	

pMUT performance across a broad range of frequencies. In Fig. 3i, the x-axis is the distance, and the y-axis is the pressure output. The frequency information is color-coded for devices from 20 to 150 kHz. Different piezoelectric materials are indicated with various markers. From the results, the KNN pMUT stands out with its transmission outputs 5 to 10 times higher than those of AlN pMUTs, and better than those of PZT-based pMUTs reported in these literature. This highlights its exceptional advantage of achieving high SPL under a low-driving voltage.
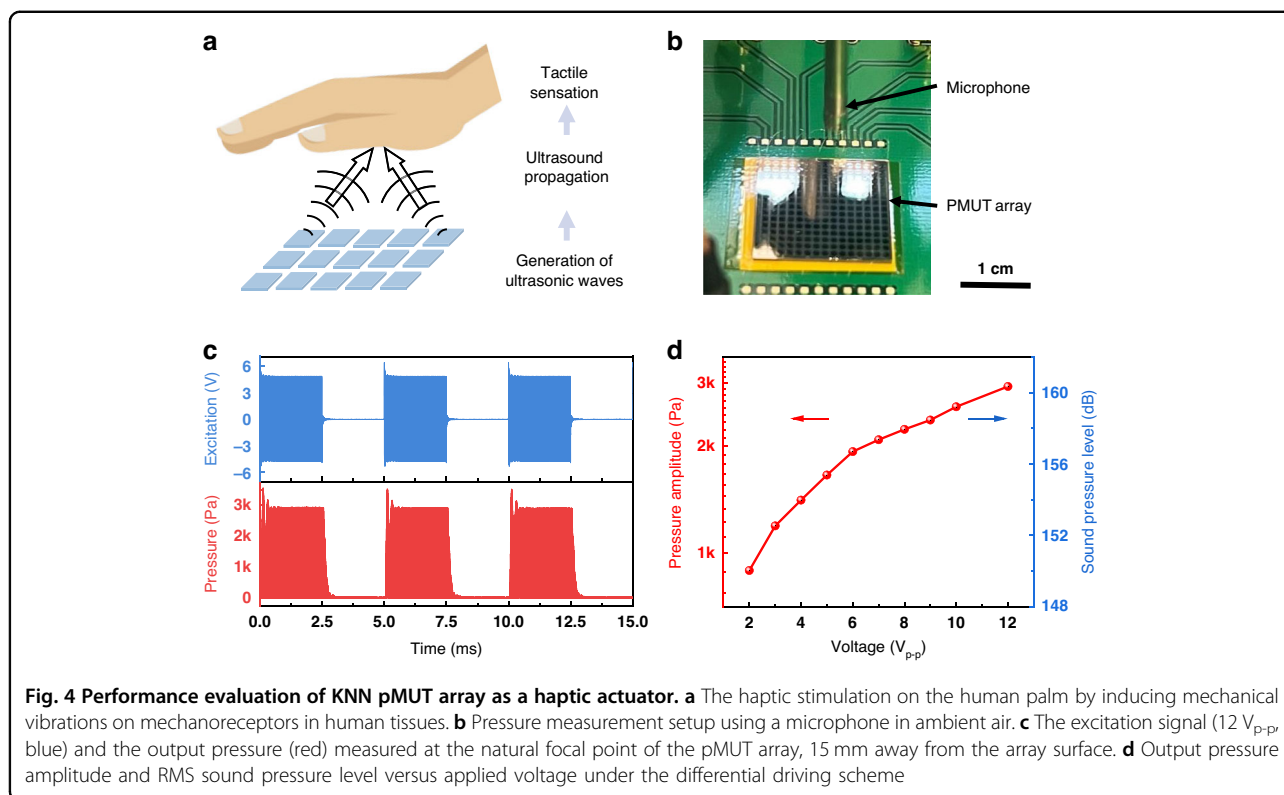
Mid-air haptic application

Haptic interfaces can enrich human-machine interactions by providing tactile feedback via the stimulation of mechanoreceptors located beneath the skin. Current haptic actuators, including the eccentric rotating mass (ERM) and linear resonant actuator (LRA), utilize electromagnetic force to produce low-frequency vibrations (<1 kHz). These actuators typically face limitations on operating within a narrow frequency range and exhibit significant actuation time lag[53]. Recently, mid-air haptic stimulation has gained interest for its advantages in fast actuation, fine spatiotemporal resolution[54], and immunity from skin surface variations. Touchless haptic systems based on bulk ultrasonic transducers, however, have a very large form factor (tens of centimeters in width), which is unsuitable for hand-held or wearable applications. Haptic actuators based on AlN pMUTs[17,18], PVDF-based pMUTs[19,55], and LiNbO$_3$ pMUTs[56] have been reported. For example, a 12×12 AlN pMUT array[17] with a resonant frequency of 109.4 kHz can generate a pressure amplitude of 950 Pa at 15 mm away under a 20 V_{p-p} excitation. By focusing the acoustic waves, a polymeric P(VDF-TrFE) annular pMUT array[55], resonating at 390 kHz, can generate a focal pressure of 1600 Pa at 20 mm away under a 63 V_{p-p} excitation. However, the acoustic output pressure of these devices is limited due to

the intrinsically small piezoelectric coefficient $e_{31,f}$ of active materials, resulting in a vague tactile sensation.

Here, we present a mid-air haptic interface device enabled by an array of 15×15 KNN pMUT elements[57]. As illustrated in Fig. 4a, the ultrasonic waves generated by the pMUT array propagate through the air and induce vibrations on the mechanoreceptors upon reaching the air-skin interface, thereby generating tactile sensations. The prototype pMUT array covers a total area of 2 cm by 2 cm, and the pressure field evaluation reveals that the natural focal point of the array without beam focusing is ~15 mm from the diaphragm surface, as shown in Fig. 4b. The output pressure evaluations are also conducted in the focal area to maximize performance. The transmitted ultrasound is modulated to low-frequency signals via the pulse-width modulation (PWM) scheme, as the ultrasound frequency signals are not perceptible to mechanoreceptors. As shown in Fig. 4c, the excitation signal features a 92.4 kHz carrier frequency, which corresponds to the resonant frequency of the pMUT array. This signal is modulated to 200 Hz, which lies within the more sensitive frequency range of mechanoreceptors[58]. Both carrier and modulation signals are rectangular waves. The modulation signal features a 50% duty cycle from prior research for optimal sensation results[17,59], which corresponds to a pulse width of 2.5 ms within a 5-ms period. The transmission performance is analyzed under various voltages, with results summarized in Fig. 4d. The focal pressure amplitude increases from 896 Pa at 2 V_{p-p} to 2900 Pa at 12 V_{p-p}, which corresponds to an RMS sound pressure level of around 160.3 dB SPL. This represents the highest output pressure achieved using an airborne pMUT array as a mid-air haptic actuator. Additionally, with a driving voltage of only 12 V_{p-p}, the transmitting sensitivity of 120.8 Pa/cm^2/V is at least two times greater than that of AlN pMUTs at a similar frequency[17]. Since the achieved pressure exceeds the minimum sensing threshold of 1 kPa[18], instant non-contact haptic

Fig. 4 Performance evaluation of KNN pMUT array as a haptic actuator. a The haptic stimulation on the human palm by inducing mechanical vibrations on mechanoreceptors in human tissues. **b** Pressure measurement setup using a microphone in ambient air. **c** The excitation signal (12 V_{p-p}, blue) and the output pressure (red) measured at the natural focal point of the pMUT array, 15 mm away from the array surface. **d** Output pressure amplitude and RMS sound pressure level versus applied voltage under the differential driving scheme

stimulation, producing a wind-like sensation on human palms, has been realized in 90% of the volunteer tests[57]. The transmission outputs of the array can be further enhanced by increasing process uniformity across the wafer. Additionally, beamforming strategies can be utilized to focus the acoustic waves and improve the efficiency in acoustic energy utilization. Beamforming can be implemented by optimizing the array design and employing a multi-channel control scheme for customized excitation. Moreover, the focused beam can be steered in one or two dimensions through amplitude and phase engineering. This capability would enable more diverse haptic stimulation patterns.
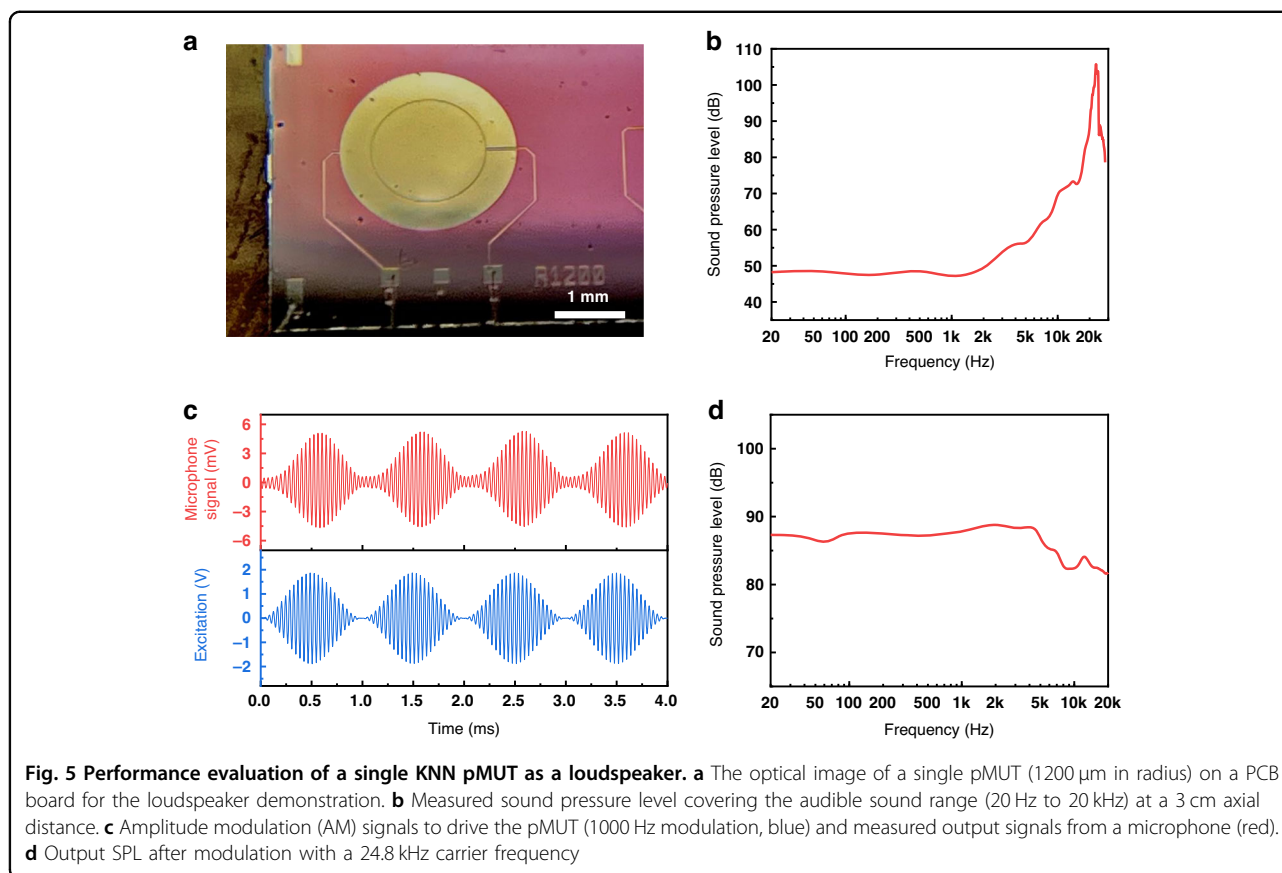
Loudspeaker application

MEMS loudspeakers have attracted extensive interest due to their small form factors, low power consumption, and ease of integration with analog front ends[60]. Unlike conventional loudspeakers, which rely on large components such as coils and magnets, MEMS loudspeakers can be realized by microfabrication processes with piezoelectric thin films as the active components. Here, we demonstrate the potential of KNN pMUTs as loudspeakers through a single pMUT element. A single pMUT with a resonant frequency close to the audible sound range is designed with a diaphragm radius of 1200 μm (Fig. 5a). Figure 5b shows the experimental frequency responses under a 4 V_{p-p}

excitation, where a high SPL of 105 dB can be achieved near the resonant frequency of 22.8 kHz at a 3 cm axial distance. The SPL remains above 46 dB throughout the audible frequency range from 20 Hz to 20 kHz. With proper structure optimization[61] and acoustic packaging[62], a more uniform frequency response could be achieved.

An alternative way to achieve audible sound through ultrasonic transducers is signal modulation and utilizing the nonlinear acoustic effect[63], such as amplitude modulation[64], which is also a way to realize directional loudspeakers. Figure 5c shows the amplitude modulation scheme commonly used in parametric arrays[65]. For better reliability and to avoid buckling, we choose to operate this pMUT at 24.8 kHz under a 4 V_{p-p} excitation, which is slightly higher than its resonant frequency. By modulating this high-frequency carrier wave ($f_c = 24.8 kHz$) with the audible-frequency modulating wave f_m, the dual-band excitation signal can be constituted as[66]:

$$y_m(t) = A\sin(2\pi f_c t) + \tfrac{1}{2}Am[\sin(2\pi(f_c + f_m)t + \phi) + \sin(2\pi(f_c - f_m)t - \phi)]$$

$$(5)$$

where A and m are the amplitude of the carrier wave and modulation wave, respectively, and ϕ is the phase of the modulating signal. The $f_c + f_m$, f_c and $f_c - f_m$ components will interact with each other through the nonlinear
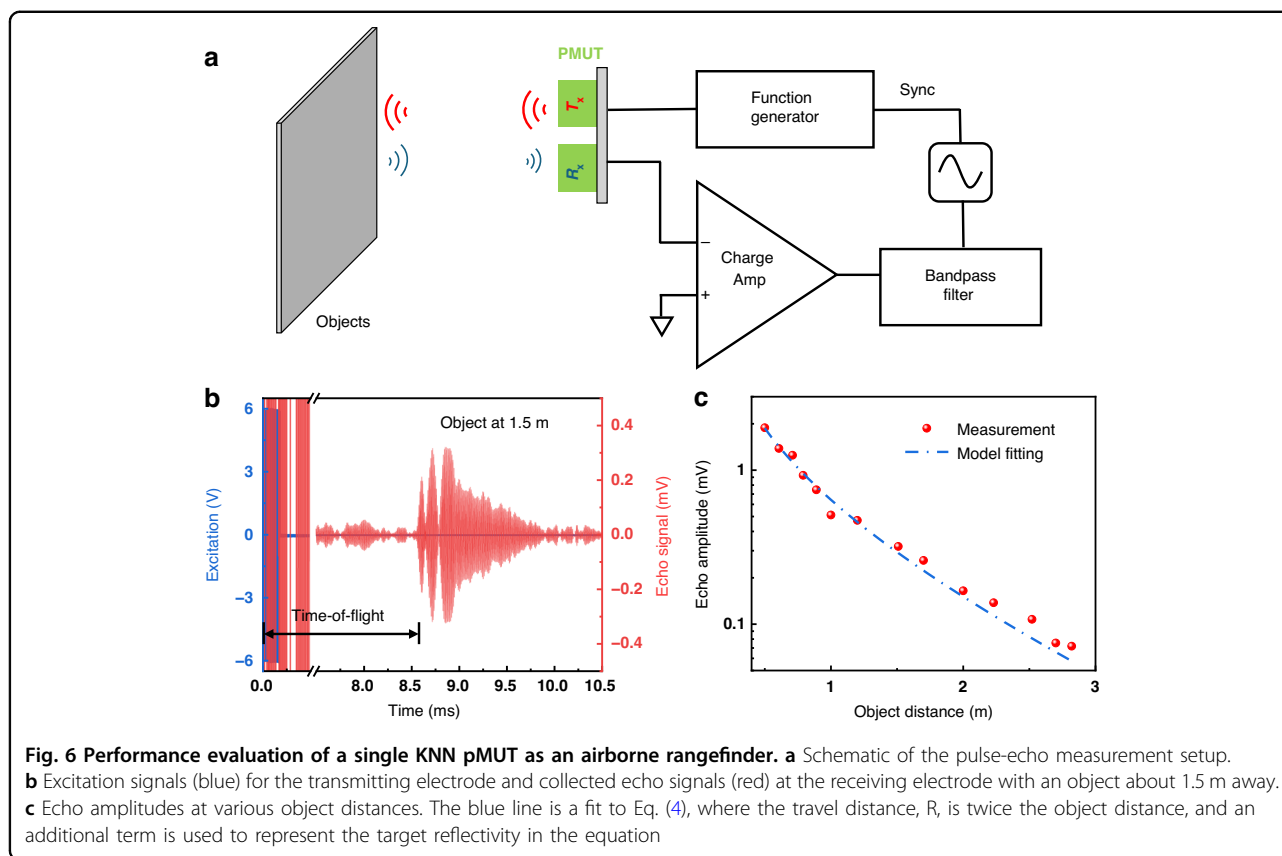
Fig. 5 Performance evaluation of a single KNN pMUT as a loudspeaker. a The optical image of a single pMUT (1200 μm in radius) on a PCB board for the loudspeaker demonstration. **b** Measured sound pressure level covering the audible sound range (20 Hz to 20 kHz) at a 3 cm axial distance. **c** Amplitude modulation (AM) signals to drive the pMUT (1000 Hz modulation, blue) and measured output signals from a microphone (red). **d** Output SPL after modulation with a 24.8 kHz carrier frequency

effect of the air[67] and generate low-frequency audible sound. This audible sound can be confirmed through the envelope of the output pressure measured at 3 cm axial distance after digital filtering. Furthermore, we take the amplitude of the envelope signal to evaluate the generated audible sound. The frequency response of the modulated signal is illustrated in Fig. 5d, indicating that the single KNN pMUT can generate a uniform acoustic output with an SPL of around 85 dB (with a deviation of ±3 dB) when modulated within the audible frequency band of 20 Hz–20 kHz. In brief, these results show that the KNN pMUT can effectively generate acoustic signals in the audible sound range. Although this structure is not optimized for speaker applications, the successful generation of audible sound demonstrates the strong output of the KNN pMUT. With further structure designs, such as suspension-spring design[61], or cantilever plate design[68] and package optimizations, such as back-chamber design[69], the KNN pMUT has the potential to exhibit high SPL and a flat frequency response.

Airborne rangefinder application

Apart from functioning as acoustic transmitters, ultrasonic transducers can sense incident ultrasounds. Ultrasound Time-of-Flight (ToF) sensors record the propagation time of a transmitted signal as it reaches a target and reflects back. This process is not affected by light conditions or the colors of targets, making them ideal for object detection, distance measurements, and positioning[70]. Recently, air-coupled pMUTs have shown great potential as ultrasonic rangefinders in consumer electronics, such as low-power presence sensing[71] and AR/VR applications[10]. The detection range depends on the transducer's transceiving sensitivity, the noise floor of the readout electronics, and the acoustic path loss during propagation[72]. The transceiving sensitivity of a ToF sensor is proportional to $\frac{e_{31,f}^2}{\varepsilon_r}$. AlN-based rangefinders are limited in transmission due to their small piezoelectric coefficient $e_{31,f}$, whereas PZT-based rangefinders suffer from low receiving performance due to their high dielectric constant ε_r. In contrast, the high $e_{31,f}$ and relatively low ε_r of KNN make it promising to extend the operation distance. Here, we characterize the performance of KNN pMUTs as an airborne rangefinder via pulse-echo measurements with a single KNN pMUT. The outer electrode serves as the transmitter, and the inner electrode works as the receiver to ensure a resonant frequency match. As previously discussed, a high-frequency ultrasound wave typically yields a high output pressure, but experiences greater acoustic path loss due to rapid attenuation during propagation. Additionally, higher

Fig. 6 Performance evaluation of a single KNN pMUT as an airborne rangefinder. a Schematic of the pulse-echo measurement setup.
b Excitation signals (blue) for the transmitting electrode and collected echo signals (red) at the receiving electrode with an object about 1.5 m away.
c Echo amplitudes at various object distances. The blue line is a fit to Eq. (4), where the travel distance, R, is twice the object distance, and an additional term is used to represent the target reflectivity in the equation

frequencies can provide better temporal and lateral resolutions due to their shorter wavelengths. In this demonstration, we use a KNN pMUT element with a radius of 500 μm that was characterized in earlier sections. For practical applications, the operation frequency depends on a proper balance among output pressure, attenuation rate, and detection resolution.

The setup for pulse-echo measurement is shown in Fig. 6a. A plastic board is used as an object to reflect pulsed ultrasound signals emitted by the pMUT transmitter, and the corresponding echo signals from the receiver are collected by an oscilloscope after being processed by a charge amplifier and bandpass filter. During the measurement, the transmitting electrode is driven by a 19-cycle pulsed square wave (102.7 kHz, 12 V_{p-p}), and the receiver signal is constantly monitored. To determine the detection range, the object distance is extended until the echo signal merges with the noise floor and the undesired reflections from the surrounding environment. An example echo signal is shown in Fig. 6b when the object is 1.5 m away. The echo has a magnitude of 0.32 mV and a ToF around 8.6 ms, which is calculated so that the received echo signal is at least 2 times larger than the baseline signal. The pMUT can detect up to a distance of 2.82 m (Fig. 6c), demonstrating its good pulse-echo sensing ability. The echo amplitude decay also matches the

model in Eq. (4). The travel distance R is twice the object distance, and an additional target reflectivity term[52] should be added. To further extend the sensing range, we can design an array of pMUT elements[33,73] to improve transmission outputs and widen the field of view. The readout electronics can be customized to enhance the SNR[52]. Developing suitable acoustic packages[72,74], such as exponential horn[72] and tube resonator[74], is another way to further improve the range by enhancing the acoustic coupling with the medium.

Conclusions

This work demonstrates sputtered KNN-based pMUTs, with the KNN film exhibiting good crystal quality in the 001 orientation for the high piezoelectric coefficient. A single KNN pMUT with a resonant frequency of 106.3 kHz under 4 V_{p-p} is used to evaluate the transmission performances and obtains a large vibration amplitude of up to 3.74 μm/V and velocity of 2.52 m/s/V. Benefiting from the high surface velocity, a transmission pressure of 132.3 dB SPL can be obtained at an axial distance of 1 cm and 111.6 dB at an axial distance of 10 cm. The corresponding transmission sensitivity is 5–10 times higher than those of state-of-the-art AlN-based pMUTs. Further research could include structural design to enhance the multi-domain coupling effects with expanded bandwidth,

packaging designs to improve acoustic coupling with the environment, customized electronics to improve driving efficiency, and environmental sensitivity and long-term reliability study for practical applications.

Potential applications such as haptic actuators, loudspeakers, and rangefinders have been demonstrated and discussed. For the haptic application, a 15×15 KNN pMUT array achieves a focal pressure amplitude of 2900 Pa. This could be further enhanced by optimizing the array design or applying beamforming techniques. For the loudspeaker application, a single pMUT element with a resonant frequency near the audible range demonstrates stable acoustic output by the amplitude modulation scheme. For the airborne rangefinder application, the pulse-echo measurements of a single pMUT element exhibit excellent sensing capabilities, maintaining a distinguishable echo signal at distances up to 2.82 m. As such, this work sheds light on high-SPL and low-driving-voltage pMUTs for potential applications in various fields where high acoustic pressure and compact form factors are favorable. Potential applications include acoustic cooling, portable and wearable ultrasound imaging, cardiovascular and edema monitoring, intravascular ultrasound (IVUS), external and interstitial high-intensity focused ultrasound (HIFU), non-destructive testing, flowmeter, underwater imaging, particle manipulation, and acoustic tweezers.

Materials and methods
Simulation method

Finite element analysis (FEA) is used to create a simulation model in COMSOL Multiphysics® v. 5.6 with three domains: Solid Mechanics to simulate the deformation of the diaphragm (fixed boundary condition), Electrostatics to simulate the internal electric field across the piezoelectric material, and Pressure Acoustics to simulate the propagation of sound waves. The Piezoelectric Effect and the Acoustic-Structure Boundary multiphysics components are applied to generate sound waves by the diaphragm. A 2D axisymmetric model is adopted to reduce computational complexity, as demonstrated in Fig. S1, due to the geometric symmetry. Free triangular meshes are used with a maximum size of one-tenth of the sound wave wavelength. A 420-μm-radius diaphragm is used as the model with a 2-μm-thick KNN layer and a 5-μm-thick silicon structural layer. Young's modulus, density, and Poisson's ratio of the KNN layer are set to 65 GPa, 4000 kg/m^3, and 0.32, respectively, with the piezoelectric coefficient $e_{31,f}$ at -8 C/m^2. The silicon structural layer is set to have a Young's modulus of 169 GPa, a density of 2320 kg/m^3, and a Poisson's ratio of 0.22. A voltage of 200 mV$_{\text{p-p}}$ is applied on the two regions of the top electrode by using the differential drive mechanism with the bottom electrode grounded to 0 V. The acoustic domain

has a hemispherical air region with a radius of 50 mm, with the infinite far-field set at a radius of 40 mm centered on the KNN layer. Frequency domain analysis is conducted between 80 and 120 kHz to solve for the resonant frequencies and the displacement of the diaphragm.

Experimental setup

During the experiments, the pMUT chips are affixed to a printed circuit board (PCB) using tapes, and the electrodes are connected to the gold (Au) contacts on the PCB via an aluminum (Al) wire-bonding process. There are two driving schemes. When the differential driving scheme is used, the bottom electrodes are grounded, and the excitation signals applied to the inner and outer top electrodes have a 180° phase shift. When only the inner electrode is used, the outer electrode is left unconnected. To evaluate the mechanical characteristics, a single-beam laser Doppler vibrometer (LDV, Polytec VibroOne) is used to capture the displacement and velocity information[75], which is then recorded by a data acquisition system (PicoScope, 5000 series) with the experimental platform shown in Fig. S2a. The laser point is focused on the center of the diaphragm in Fig. S2b, and the measurement chamber is isolated from the ambient environment to minimize interferences. The raw data captured from the LDV is presented in the format of voltage, corresponding to the preset velocity sensitivity (options used: 500 mm/s/V or 5 m/s/V) and displacement sensitivity (options used: 500 nm/V, 5 μm/V, or 50 μm/V). Both sensitivities are adjusted accordingly based on the amplitude of the captured data. These raw data are subsequently converted into displacement and velocity information during post-signal processing. The quality factor (Q) is calculated based on the -6 dB bandwidth from the displacement frequency response. To characterize the acoustic performance, a microphone (Bruel & Kjar, Type 4138) equipped with a preamplifier (Type 1708) is used to measure the output pressure, as shown in Fig. S3. The raw microphone signal is recorded by the data acquisition system as voltages and then converted to pressure (Pa) using the microphone sensitivity (0.719 mV/Pa) and free-field calibrations. The sound pressure level is calculated from the root mean square (RMS) pressure amplitude based on the following equation:

$$\text{SPL} = 20\log_{10}\left(\frac{P}{P_0}\right)$$

Where P is the measured sound pressure amplitude, and P_0 is the reference sound pressure, which is 20 μPa in air.

processes, and the UC Berkeley Marvell Nanofabrication Lab for the rest of the fabrication process. The authors would like to acknowledge Xiaoyu Niu from the University of Texas at Austin and Tahmid Kaisar from the University of Florida for their insightful suggestions and discussions. The authors would like to thank Dr. Wen Sui, Haotian Lu, and Prof. Xiaoyu (Rayne) Zheng for their assistance with testing. The work of M.A. and L.W.M. was sponsored by the Army Research Laboratory and was accomplished under Cooperative Agreement Number W911NF-24-2-0100. The views and conclusions contained in this document are those of the authors and should not be interpreted as representing the official policies, either expressed or implied, of the Army Research Laboratory or the US Government. The US Government is authorized to reproduce and distribute reprints for Government purposes, notwithstanding any copyright notation herein.

Author details

^{1}Department of Mechanical Engineering, University of California, Berkeley, CA 94720, USA. ^{2}School of Electronic Science and Engineering, Southeast University, Nanjing, Jiangsu 210096, China. ^{3}Bioengineering and Biomedical Engineering, Xi'an Jiaotong University, Xi'an, Shaanxi 710049, China. ^{4}Tsinghua Shenzhen International Graduate School, Tsinghua University, Shenzhen 518055, China. ^{5}Department of Materials Science and Engineering, University of California, Berkeley, CA 94720, USA. ^{6}Scientific Research Laboratory Div., Niterra Co., Ltd, Nagoya 461-0005, Japan. ^{7}Departments of Materials Science and NanoEngineering, Chemistry, and Physics and Astronomy and the Rice Advanced Materials Institute, Rice University, Houston, TX 77005, USA

Author contributions

F.X., Y.P., S.P., R.A., and L.L. conceived the concept. L.L. and L.W.M. provided guidance and support for the research. F.X., S.P., Y.P., and R.A. designed and developed the devices. W.Y., F.X., and Y.P. performed the simulation analysis. F.X., Y.P., M.L., M.T., C.M.C., X.Y., Y.M., and M.A. contributed to the experiments. F.X. and Y.P. carried out data analysis. F.X., Y.P., W.Y., M.T., L.W.M., and L.L. participated in the manuscript writing. All authors contributed through scientific discussions.

Conflict of interest

The authors declare no competing interests.

References

1. Shoval, S. & Borenstein, J. Using coded signals to benefit from ultrasonic sensor crosstalk in mobile robot obstacle avoidance. *Proc. IEEE Int. Conf. Robot Autom.* **3**, 2879–2884 (2001).
2. Drinkwater, B. W. & Wilcox, P. D. Ultrasonic arrays for non-destructive evaluation: a review. *NDT E Int.* **39**, 525–541 (2006).
3. Jiang, X., Kim, K., Zhang, S., Johnson, J. & Salazar, G. High-temperature piezoelectric sensing. *Sensors* **14**, 144–169 (2013).
4. Hunt, J. W., Arditi, M. & Foster, F. S. Ultrasound transducers for pulse-echo medical imaging. *IEEE Trans. Biomed. Eng.* **BME-30**, 453–481 (1983).
5. Synnevåg, J. F., Austeng, A. & Holm, S. Adaptive beamforming applied to medical ultrasound imaging. *IEEE Trans. Ultrason. Ferroelectr. Freq. Control* **54**, 1606–1613 (2007).
6. Leinenga, G., Langton, C., Nisbet, R. & Götz, J. Ultrasound treatment of neurological diseases - current and emerging applications. *Nat. Rev. Neurol.* https://doi.org/10.1038/nrneurol.2016.13 (2016).
7. Ter Haar, G. R. High intensity focused ultrasound for the treatment of tumors. *Echocardiography* **18**, 317–322 (2001).
8. Przybyla, R. J. et al. In-air rangefinding with an AlN piezoelectric micromachined ultrasound transducer. *IEEE Sens. J.* **11**, 2690–2697 (2011).
9. Chen, X., Xu, J., Chen, H., Ding, H. & Xie, J. High-accuracy ultrasonic rangefinders via pMUTs arrays using multi-frequency continuous waves. *J. Microelectromech. Syst.* **28**, 634–642 (2019).
10. Przybyla, R. J., Tang, H. Y., Shelton, S. E., Horsley, D. A. & Boser, B. E. 3D ultrasonic gesture recognition. In *Digest of Technical Papers - IEEE International Solid-State Circuits Conference* 210–211 (2014).
11. Gijsenbergh, P. et al. Characterization of polymer-based piezoelectric micromachined ultrasound transducers for short-range gesture recognition applications. *J. Micromech. Microeng.* **29**, 074001 (2019).
12. Jiang, X. et al. Ultrasonic fingerprint sensor with transmit beamforming based on a PMUT array bonded to CMOS circuitry. *IEEE Trans. Ultrason. Ferroelectr. Freq. Control* **64**, 1401–1408 (2017).
13. Lu, Y. et al. Ultrasonic fingerprint sensor using a piezoelectric micromachined ultrasonic transducer array integrated with complementary metal oxide semiconductor electronics. *Appl. Phys. Lett.* **106**, 263503 (2015).
14. Shao, Z., Peng, Y., Pala, S., Liang, Y. & Lin, L. 3D ultrasonic object detections with >1 meter range. In *Proc. IEEE International Conference on Micro Electro Mechanical Systems (MEMS)* 386–389 (Institute of Electrical and Electronics Engineers Inc., 2021).
15. Wu, H. et al. An ultrasound ASIC with universal energy recycling for >7-m all-weather metamorphic robotic vision. *IEEE J. Solid State Circuits* **57**, 3036–3047 (2022).
16. Shao, Z., Pala, S., Peng, Y. & Lin, L. Bimorph pinned piezoelectric micromachined ultrasonic transducers for space imaging applications. *J. Microelectromech. Syst.* **30**, 650–658 (2021).
17. Pala, S., Shao, Z., Peng, Y. & Lin, L. Ultrasond-induced haptic sensations via PMUTS. In *Proc. IEEE International Conference on Micro Electro Mechanical Systems (MEMS)* 911–914 (Institute of Electrical and Electronics Engineers Inc., 2021).
18. Billen, M. et al. PMUT array design for mid-air haptic feedback. In *2022 23rd International Conference on Thermal, Mechanical and Multi-Physics Simulation and Experiments in Microelectronics and Microsystems (EuroSimE)* 1–6 (IEEE, 2022).
19. Halbach, A. et al. Display compatible PMUT array for mid-air haptic feedback. In *2019 20th International Conference on Solid-State Sensors, Actuators and Microsystems & Eurosensors XXXIII (TRANSDUCERS & EUROSENSORS XXXIII)* 158–161 (IEEE, 2019).
20. Shao, Z., Pala, S., Liang, Y., Peng, Y. & Lin, L. A Single chip directional loudspeaker based on PMUTS. In *Proc. IEEE International Conference on Micro Electro Mechanical Systems (MEMS)* 895–898 (Institute of Electrical and Electronics Engineers Inc., 2021).
21. Je, Y., Lee, H., Been, K. & Moon, W. A micromachined efficient parametric array loudspeaker with a wide radiation frequency band. *J. Acoust. Soc. Am.* **137**, 1732–1743 (2015).
22. Ozcelik, A. et al. Acoustic tweezers for the life sciences. *Nat. Methods* https://doi.org/10.1038/s41592-018-0222-9 (2018).
23. Sammoura, F., Shelton, S., Akhbari, S., Horsley, D. & Lin, L. A two-port piezoelectric micromachined ultrasonic transducer. In *2014 Joint IEEE International Symposium on the Applications of Ferroelectric, International Workshop on Acoustic Transduction Materials and Devices & Workshop on Piezoresponse Force Microscopy* 1–4 (IEEE, 2014).
24. Akhbari, S., Sammoura, F., Eovino, B., Yang, C. & Lin, L. Bimorph piezoelectric micromachined ultrasonic transducers. *J. Microelectromech. Syst.* **25**, 326–336 (2016).
25. Guedes, A. et al. Aluminum nitride pMUT based on a flexurally-suspended membrane. In *2011 16th International Solid-State Sensors, Actuators and Microsystems Conference, TRANSDUCERS'11* 2062–2065 (2011).
26. Ledesma, E., Zamora, I., Uranga, A. & Barniol, N. Tent-plate AlN PMUT with a piston-like shape under liquid operation. *IEEE Sens. J.* **20**, 11128–11137 (2020).
27. Wang, T., Sawada, R. & Lee, C. A piezoelectric micromachined ultrasonic transducer using piston-like membrane motion. *IEEE Electron Device Lett.* **36**, 957–959 (2015).
28. Akhbari, S. et al. Self-curved diaphragms by stress engineering for highly responsive pMUT. In *Proc. IEEE International Conference on Micro Electro Mechanical Systems (MEMS)* 837–840 (Institute of Electrical and Electronics Engineers Inc., 2015).
29. Wang, T., Kobayashi, T. & Lee, C. Micromachined piezoelectric ultrasonic transducer with ultra-wide frequency bandwidth. *Appl. Phys. Lett.* **106**, 013501 (2015).
30. Sammoura, F., Smyth, K. & Kim, S. G. Optimizing the electrode size of circular bimorph plates with different boundary conditions for maximum deflection of piezoelectric micromachined ultrasonic transducers. *Ultrasonics* **53**, 328–334 (2013).

31. Liang, Y., Eovino, B. & Lin, L. Piezoelectric micromachined ultrasonic transducers with pinned boundary structure. *J. Microelectromech. Syst.* **29**, 585–591 (2020).

32. Pala, S. & Lin, L. Piezoelectric micromachined ultrasonic transducers (pMUT) with free boundary. In *2020 IEEE International Ultrasonics Symposium (IUS)* 1–4 (IEEE, 2020).

33. Kusano, Y. et al. High-SPL air-coupled piezoelectric micromachined ultrasonic transducers based on 36% ScAlN thin-film. *IEEE Trans. Ultrason. Ferroelectr. Freq. Control* **66**, 1488–1496 (2019).

34. Yang, H. et al. AlScN film based piezoelectric micromechanical ultrasonic transducer for an extended long-range detection. *Micromachines* **13**, 1942 (2022).

35. Wang, Q., Lu, Y., Mishin, S., Oshmyansky, Y. & Horsley, D. A. Design, fabrication, and characterization of scandium aluminum nitride-based piezoelectric micromachined ultrasonic transducers. *J. Microelectromech. Syst.* **26**, 1132–1139 (2017).

36. Luo, G. L., Kusano, Y. & Horsley, D. A. Airborne piezoelectric micromachined ultrasonic transducers for long-range detection. *J. Microelectromech. Syst.* **30**, 81–89 (2021).

37. Massimino, G. et al. Air-coupled PMUT at 100 kHz with PZT active layer and residual stresses: multiphysics model and experimental validation. In *2017 18th International Conference on Thermal, Mechanical and Multi-Physics Simulation and Experiments in Microelectronics and Microsystems (EuroSimE)* 1–4 (IEEE, 2017).

38. Wada, S., Yako, K., Kakemoto, H., Tsurumi, T. & Kiguchi, T. Enhanced piezoelectric properties of barium titanate single crystals with different engineered-domain sizes. *J. Appl. Phys.* **98**, 014109 (2005).

39. Simeoni, P., Schaffer, Z. & Piazza, G. A 100 nm thick, 32 kHz X-cut lithium niobate piezoelectric nanoscale ultrasound transducer for airborne ultrasound communication. *J. Microelectromech. Syst.* **30**, 337–339 (2021).

40. Pop, F., Herrera, B. & Rinaldi, M. Lithium niobate piezoelectric micromachined ultrasonic transducers for high data-rate intrabody communication. *Nat. Commun.* **13**, 1–12 (2022).

41. Zheng, T. et al. High-performance potassium sodium niobate piezoceramics for ultrasonic transducer. *Nano Energy* **70**, 104559 (2020).

42. Wakasa, Y. et al. Piezoelectric properties of microfabricated (K,Na)NbO3 thin films. *Sens. Actuators A Phys.* **171**, 223–227 (2011).

43. Shibata, K., Watanabe, K., Kuroda, T. & Osada, T. KNN lead-free piezoelectric films grown by sputtering. *Appl. Phys. Lett.* **121**, 092901 (2022).

44. Huang, Y. et al. Implementing (K,Na)NbO3-based lead-free ferroelectric films to piezoelectric micromachined ultrasonic transducers. *Nano Energy* **103**, 107761 (2022).

45. Xia, F. et al. High-SPL and low-driving-voltage pMUTs by sputtered potassium sodium niobate. In *2023 IEEE 36th International Conference on Micro Electro Mechanical Systems (MEMS)* 135–138 (IEEE, 2023).

46. Shelton, S. et al. CMOS-compatible AlN piezoelectric micromachined ultrasonic transducers. In *2009 IEEE International Ultrasonics Symposium* 402–405 (IEEE, 2009).

47. Pala, S. & Lin, L. An improved lumped element model for circular-shape pMUTs. *IEEE Open J. Ultrason. Ferroelectr. Freq. Control* **2**, 83–95 (2022).

48. Mason, W. P. *Electromechanical Transducers and Wave Filters* (Van Nostrand, 1942).

49. Massimino, G., Lazarova, B., Quaglia, F. & Corigliano, A. Air-coupled PMUTs array with residual stresses: experimental tests in the linear and non-linear dynamic regime. *Int. J. Smart Nano Mater.* **11**, 387–399 (2020).

50. Kaisar, T., Lee, J., Li, D., Shaw, S. W. & Feng, P. X.-L. Nonlinear stiffness and nonlinear damping in atomically thin MoS$_2$ nanomechanical resonators. *Nano Lett.* **22**, 9831–9838 (2022).

51. Wang, Z. & Feng, P. X.-L. Dynamic range of atomically thin vibrating nanomechanical resonators. *Appl. Phys. Lett.* **104**, 103109 (2014).

52. Przybyla, R. J. et al. 3D ultrasonic rangefinder on a chip. *IEEE J. Solid-State Circuits* **50**, 320–334 (2015).

53. Basdogan, C., Giraud, F., Levesque, V. & Choi, S. A review of surface haptics: enabling tactile effects on touch surfaces. *IEEE Trans. Haptics* https://doi.org/10.1109/TOH.2020.2990712 (2020).

54. Wilson, G., Carter, T., Subramanian, S. & Brewster, S. Perception of ultrasonic haptic feedback on the hand: Localisation and apparent motion. In *Conference on Human Factors in Computing Systems - Proceedings* 1133–1142 (Association for Computing Machinery, 2014).

55. Chare, C. et al. High performance large-area polymeric PMUT phased arrays in air. In *2022 IEEE International Ultrasonics Symposium (IUS)* 1–4 (IEEE, 2022).

56. Yue, W. et al. Auto-positioning and haptic stimulations via a 35 mm square Pmut array. In *2023 IEEE 36th International Conference on Micro Electro Mechanical Systems (MEMS)* 941–944 (IEEE, 2023).

57. Xia, F. et al. High-SPL pMUT array for mid-air haptic interface. In *2023 22nd International Conference on Solid-State Sensors, Actuators and Microsystems (Transducers)* 124–127 (2023).

58. Henley, C. *Foundations of Neuroscience* (Michigan State University Libraries, 2021).

59. Hoshi, T., Takahashi, M., Iwamoto, T. & Shinoda, H. Noncontact tactile display based on radiation pressure of airborne ultrasound. *IEEE Trans. Haptics* **3**, 155–165 (2010).

60. Stoppel, F. et al. New integrated full-range MEMS speaker for in-ear applications. In *Proc. IEEE International Conference on Micro Electro Mechanical Systems (MEMS)* 1068–1071 (IEEE, 2018).

61. Cheng, H.-H. et al. On the design of piezoelectric MEMS microspeaker for the sound pressure level enhancement. *Sens. Actuators A Phys.* **306**, 111960 (2020).

62. Beer, D. et al. Expedition MEMS speaker. In *Forum Acusticum* 2921–2928 (2020).

63. Duck, F. A. Nonlinear acoustics in diagnostic ultrasound. *Ultrasound Med. Biol.* **28**, 1–18 (2002).

64. Zhao, H. et al. Ultrasound-based directional sound system via double sideband amplitude modulation. *IEEE Sens. J.* **23**, 17319–17328 (2023).

65. Shi, C., Kajikawa, Y. & Gan, W. S. An overview of directivity control methods of the parametric array loudspeaker. *APSIPA Trans. Signal Inform. Process.* https://doi.org/10.1017/ATSIP.2014.18 (2014).

66. Oppenheim, A. V., Willsky, A. S. & Nawab, S. H. *Signals & Systems* (Pearson Educación, 1997).

67. Nakayama, M. & Nishiura, T. Synchronized amplitude-and-frequency modulation for a parametric loudspeaker. In *2017 Asia-Pacific Signal and Information Processing Association Annual Summit and Conference (APSIPA ASC)* 130–135 (IEEE, 2017).

68. Cheng, H.-H. & Fang, W. THD improvement of piezoelectric MEMS speakers by dual cantilever units with well-designed resonant frequencies. *Sens. Actuators A Phys.* https://doi.org/10.1016/j.sna.2024.115717 (2024).

69. Tseng, C., Wei, T.-C., Lin, C.-H., Hu, Z.-S. & Fang, W. Using reverse-trapezoid cantilevers and sealed back-chamber to enhance the performance of mems piezoelectric microspeaker at ultra-high frequencies. In *2024 IEEE 37th International Conference on Micro Electro Mechanical Systems (MEMS)* 721–724 (IEEE, 2024).

70. Hazas, M. & Hopper, A. Broadband ultrasonic location systems for improved indoor positioning. *IEEE Trans. Mob. Comput.* **5**, 536–547 (2006).

71. Horsley, D. A. et al. Piezoelectric micromachined ultrasonic transducers in consumer electronics: the next little thing? In *2016 IEEE 29th International Conference on Micro Electro Mechanical Systems (MEMS)* 145–148 (IEEE, 2016).

72. Przybyla, R. J. et al. Mass produced micromachined ultrasonic time-of-flight sensors operating in different frequency bands. In *2023 IEEE 36th International Conference on Micro Electro Mechanical Systems (MEMS)* 961–964 (IEEE, 2023).

73. Peng, Y. et al. 9-meter-long 3 d ultrasonic objects detection via packaged lithium-niobate PMUTs. In *2024 IEEE 37th International Conference on Micro Electro Mechanical Systems (MEMS)* 124–127 (IEEE, 2024).

74. Shelton, S. et al. Improved acoustic coupling of air-coupled micromachined ultrasonic transducers. In *2014 IEEE 27th International Conference on Micro Electro Mechanical Systems (MEMS)* 753–756 (IEEE, 2014).

75. Acharya, M. et al. Direct measurement of inverse piezoelectric effects in thin films using laser doppler vibrometry. *Phys. Rev. Appl.* **20**, 014017 (2023).

76. Schneider, M., Dorfmeister, M., Moll, P., Kaltenbacher, M. & Schmid, U. Bi-stable aluminum nitride-based piezoelectric micromachined ultrasonic transducer (PMUT). *J. Microelectromech. Syst.* **29**, 948–953 (2020).

77. Wang, T., Kobayashi, T. & Lee, C. Highly sensitive piezoelectric micromachined ultrasonic transducer operated in air. *Micro Nano Lett.* **11**, 558–562 (2016).

78. Zhou, Z., Yoshida, S. & Tanaka, S. Epitaxial PMnN-PZT/Si MEMS ultrasonic rangefinder with 2 m range at 1 V drive. *Sens. Actuators A Phys.* **266**, 352–360 (2017).